PEER REVIEWED

Effect of Nanostructure on Wear and Corrosion Behavior of HVAF-Sprayed Eutectic High-Entropy Alloy Coatings

Shuyu Liu[1] · Yingbo Peng[1,2] · Yong Zhang[1,3] · Yueming Wang[4] · Weijie Fan[3] · Andong Wang[3] · Wei Zhang[1] · Yanni Tan[1] · Qingyuan Ma[1] · Yang Lan[1]

Abstract Adopting multi-principal high entropy alloys (HEAs) as wear/corrosion-resistant coatings is a frontier in the field of surface engineering. The eutectic high entropy alloy (EHEA) exhibited excellent mechanical properties, and its dual-phase, lamellar nanostructure effectively prohibited pitting corrosion, making the alloy a potential candidate for wear/corrosion-resistant coatings served in the complicated environments. In the presented study, a dense and non-oxidized CoCrFeNiTaAl EHEA was coated on 304 stainless steel (SUS 304) substrate by a high-velocity air fuel (HVAF) thermal spraying process. The microstructure, corrosion resistance, as well as high temperature wear resistance of the coating were analyzed. The coating consisted of a deformation zone and a solidified zone. The deformation zone had the same structure as the original powders of the hypo-eutectic structure, and the solidified zone exhibited a single-phase solid solution structure. The EHEA coating exhibited an excellent combination of pitting corrosion and room-temperature wear resistance. The wear mechanism of EHEA coatings was abrasive, and oxidation wear at room temperature and 100 °C, while adhesive and oxidation wears occurred at elevated temperatures. The wear resistance decreases as temperature increases.

Keywords coating · corrosion · high entropy alloy · HVAF · microstructures · wear

✉ Wei Zhang
waycsu@csu.edu.cn

1 State Key Laboratory of Powder Metallurgy, Central South University, Changsha 410083, China

2 College of Engineering, Nanjing Agricultural University, Nanjing 210031, China

3 Qingdao Branch of Naval Aeronautical University, Qingdao 266041, China

4 Hunan Provincial Key Laboratory of High Efficiency and Precision Machining of Difficult-to-Cut Material, Hunan University of Science and Technology, Xiangtan 411201, China

Introduction

The protection of metallic parts in the ocean environment is of great research interest to marine engineering. Because of its low corrosion rate and good mechanical properties, stainless steel is commonly used as pumps, valves, fastening rods, and other moving parts in the marine environment, facing the challenges of corrosion and wear. However, the poor Cl ion pitting resistance and wear resistance of stainless steel severely limit its application, especially some parts exposed to high temperature in the salt-fog scenario. For example, in an aero-engine of carrier-borne aircraft, the contact part between compressor blades and compressor disk would have friction with a temperature of more than 400 °C. Meanwhile, these compressor components would also be corroded by marine salt fog. Thus, to improve the service performance and extend the service life of the working pieces, coating technology is considered to be economical and effective (Ref 1-3).

High entropy alloys (HEAs) have great application potentials due to their excellent properties, including hardness, ductility, strength, (Ref 4-6), and corrosion resistance (Ref 7-9). Recent research on using high entropy alloys as surface modification materials has attracted great attention (Ref 10-15). HEAs is generally considered to have good corrosion resistance. The general thickness loss rate of $CuCr_2Fe_2Ni_2Mn_2$ is only 4% of 304 stainless steel under acidic conditions (Ref 16). On the other hand, HEAs coatings with improved wear resistance are usually obtained by alloying with other elements and in-situ formed second phase. The reported wear rates of $(CoCrFeMnNi)_{85}Ti_{15}$ (Ref 13), $AlCoCrFeNiTi_{0.5}$ (Ref 14) and MoFeCrTiWAlNb (Ref 17) were significantly lower than that of 304 stainless steel. However, the improvement of wear resistance caused by second-phase strengthening is detrimental to corrosion resistance (Ref 18, 19).

The design strategy of dual-phase eutectic high entropy alloys (EHEAs) achieves excellent comprehensive mechanical properties (Ref 20, 21). Moreover, it promises to eliminate the contradiction between corrosion resistance and wear resistance. Researchers discovered that due to the compact chemically passive film with the nanostructure, excellent corrosion resistance of $FeCrNiCoNb_{0.5}$ can be obtained, especially pitting corrosion resistance (Ref 22). Moreover, it is found that lamellar eutectic EHEAs consisting of FCC and Laves phase have good wear resistance (Ref 23). The wear resistance of $CoCrFeNiNb_x$ EHEA is significantly improved than that of 304 stainless steel (Ref 24). In addition, the reported CoCrFeNiTaAl EHEA has good mechanical properties at elevated temperatures (Ref 25). Thus, these ideal performances make the EHEAs a potential candidate for high-performance protective coating materials in marine applications.

HEA coatings prepared by laser cladding and thermal spray have been studied extensively (Ref 14, 26-30). However, the high heating/cooling rate of these traditional coating technologies are not conducive to the forming of eutectic structure. High-velocity air fuel (HVAF) can be a suitable method for EHEA coating because of the lower temperature and faster velocity of powder during the spraying process (Ref 31, 32). The lower temperature can reduce powder melting and thus prevent the eutectic structure from transforming to other non-equilibrium phases. Higher impact velocity brings significant deformation during spraying, which is beneficial to improvement of the coating density. In addition, the lower temperature and less exposure time to the atmosphere help to avoid oxidation and thus improve the cohesion of the coating (Ref 31).

In the present study, the microstructure evolution of CoCrFeNiTaAl EHEA coatings during the HVAF process was investigated, and the pitting corrosion and wear resistance of the coatings were analyzed. Further, wear resistance below 400 °C was tested to evaluate the potential of the coating for high-temperature applications. The purpose is to provide a new solution for improving the service performance and broadening the application field of 304 stainless steel (SUS 304) parts in the marine environment.

Experimental Material and Methods

Feedstock and Coating Preparation

The pre-alloyed powders of Non-equiatomic CoCrFeNi-TaAl eutectic high entropy alloy(referred to as EHEA)were prepared by a gas atomization system, and Table 1 shows the nominal chemical composition of it. Raw materials of Fe, Co, Cr, Ni, Ta, and Al whose purity is higher than 99.9%, were heated to melting in an electromagnetic induction crucible in a vacuum furnace and homogenized by electromagnetic stirring. The molten alloy was poured into an atomization chamber and cooled by argon of high purity, and then it solidified into powder. Meanwhile, the EHEA ingot for control was obtained. The powder in size between 15 and 53 μm was collected for HVAF in feeding after mechanical vibration screening and air classification. Figure 1 presents the surface morphology and the microstructure of EHEA powders. The powders show good sphericity which is a typical characteristic of gas atomized powder, and satellite particle can be seen around larger particles. The quantitative statistics of particle size were carried out by a laser particle size analyzer. The result revealed that the size range was between 15.2-59.9 μm, D50 was 30.4 μm. It matched the size requirement (15-45 μm) of the HVAF system. The high magnification images revealed that there were dendrites on the powder surface, which was typical characteristic of non-equilibrium solid-ified microstructure. The oxygen content of 0.0183 wt.% was analyzed using a nitrogen/oxygen determinator (TC600, Leco, Chicago, IL, USA), and it can be concluded almost no oxidation occurred during the gas atomization process. The DSC curve showed a unique endothermic peak at 1338.2 °C, which represented the melting point of the EHEA. This eutectic alloy has significantly lower melting points and softening temperature relative to FeCoCrNi HEA (Ref 33).

The EHEA coatings were prepared using a High-Velocity Air Fuel system (M2h, Unique Coat, USA)

Table 1 The nominal chemical composition of EHEA

Elements	Co	Fe	Ni	Cr	Ta	Al
Content, at.%	25.1	23.3	22.6	18.8	8.5	1.7
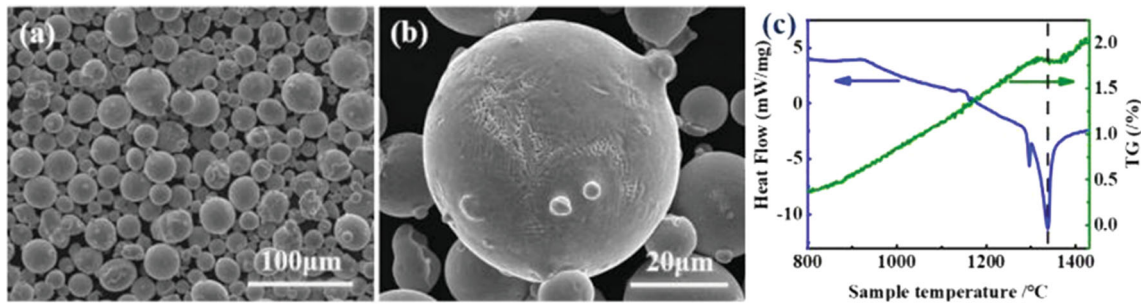
Fig. 1 Morphology (SE) of gas-atomized EHEA powders: (a) low magnification; (b) high magnification and (c) TG-DSC curves

Table 2 Parameters of the HVAF spraying process

Parameters	Value
Air pressure	0.8 MPa
Propane pressure	0.9 MPa
Powder feed rate	80 g/min
Spraying distance	360 mm
Spraying angle	90°

Table 3 Parameters of wear investigations under reciprocating conditions

Parameters	Value
Force	5 N
Rotation speed	560 r/min
Time	30 min
Rotation radius	3 mm
Counter Body	Si_3N_4
Temperature	RT, 100, 250, 400 °C

equipped with an M3[TM] gun. The system adopts air as a combustion supporting agent, propane as fuel, N_2 as feeding gas. A 304 stainless steel plate with a thickness of 9 mm was used as a substrate, and the surface was cleaned with acetone and blasted by spherical corundum with a diameter of 2mm before spraying. The parameters of the spraying process are listed in Table 2. As sprayed coating was cut into specimens by wire-cut electrical discharge machining.

Characterization

The microstructure and chemical composition of feeding powders, coating section, and friction surface were analyzed by scanning electron microscope (SEM) with back-scattering mode (FEI Quanta FEG 250, Czech) and matched energy dispersive spectrometry (EDS) probe. Powder particle size and thermogravimetric analysis were obtained by laser particle size tester (Mastersizer 3000, UK) and synchronous thermal analyzer (STA-449C, SETARAM Instrumentation, France), respectively. Image processing software (Image J) was used to calculate the porosity of the coating by analyzing the SEM images. ASTM standard E2109-01(2014) was followed to conduct the test. X-ray diffractometry (XRD, Bruck D8 Advance, Germany) with Cu-Kα radiation at 20-90° and 8°/min was used. Software MDI Jade was used to analyze each pattern, and the full-width at half of the maximum (FWHM) were obtained.

The electrochemical tests were conducted on a multi-channel electrochemical workstation (Multi Autolab M204). The tested samples were set as working electrodes, while the platinum electrode and saturated calomel electrode (SCE) were set as counter electrode and reference electrode, respectively. The measurements were carried out in 3.5 wt.% NaCl solution at 25 °C under atmospheric pressure. For potentiodynamic polarization tests, each sample was scanned at a rate of 1 mV/s from an initial potential of −0.5 V (vs. SCE) to a final potential of 0.8 V (vs. SCE). For electrochemical impedance spectroscopy (EIS) tests, an alternating current (AC) with an amplitude of 10 mV was used in the frequency range of 100 kHz to 10 mHz.

The hardness of coating, ingot, and substrate was investigated using micro Vickers with a load of 10 N for 10 seconds, and the average values were calculated from 5 measurements. Ball-plate wear testing under different temperatures was carried out in the high-temperature wear tester (GHT-1000, Lanzhou) where Si_3N_4 balls (5 mm diameter) were used as counterparts against the coated surface. The wear tests were conducted at atmospheric conditions, and the parameters were listed in Table 3. Probe-type material surface wear mark measuring instrument (MT-500, Lanzhou) was used to investigate wear scar profiles, and the volume wear was further calculated. Three parallel tests were performed on each condition, and the average of wear and friction coefficients were taken. The wear rate was counted by the following formula (Ref 34):

$$W = \frac{V}{N \cdot L} \tag{Eq 1}$$

where L was the sliding distance (m), V was the wear volume loss (mm^3) and W was the wear rate ($mm^3/N·m$), N was the applied normal load (N).

Results and Discussion

Coating Characterization

The phase of EHEA coating prepared by HVAF and feeding powders were analyzed by XRD, as shown in Fig. 2. The results show powders and coating mainly consisted of FCC phase and Laves phase (structure type of $MgZn_2$, space group 194). In the pattern of powders, the dominated FCC peaks validate the hypo-eutectic structures with primary FCC and FCC+Laves eutectic. Compared with patterns of EHEA coating and powders, it can be seen that the peak positions were very close, while the strength was quite different. Parameters of prominent peaks are shown in Table 4. It was found that the EHEA by HVAF shows additional broadening, excluding the effect of instrument broadening, which indicates a large stress in the coating. Comparing the peak areas, it can be determined that the content of Laves phase in the EHEA reduced after the HVAF process.

The microstructures of the as-sprayed coating and feeding powder were shown in Fig. 3. In Fig. 3(a), the EHEAs coating and 304 stainless steel matrix compactly bonded, and the elements in the coating distributed uniformly. SEM images (SE) of the coating were analyzed by image processing software, and the porosity of the coating was confirmed to be 0.13%, representing almost full-dense coating. As shown in Fig. 3(b) and (c), the coating consisted of two types of microstructures, where one is oblate or spherical, and the other fills the gaps. Similar to feeding
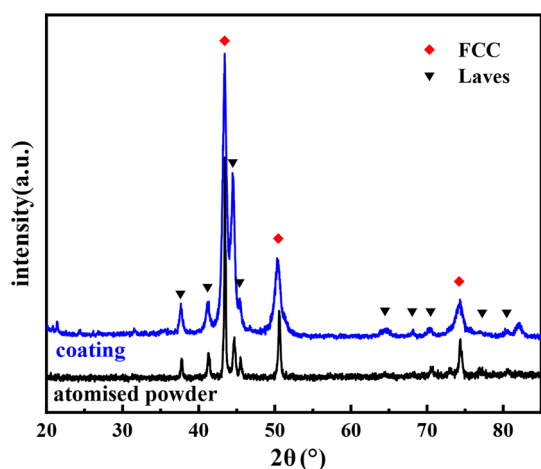
Fig. 2 XRD patterns of as-sprayed coating and gas-atomized powder of EHEA

powders, there were multiphase structures at a nanometer scale in the main structure, as shown in Fig. 3(c) and (d). This nanostructure exhibits a typical dendritic hypoeutectic structure. In the process of HVAF spraying, the nanostructure of powder was retained in the coating with severe deformation, reflecting the heritability of the process. The microstructure composed of deformed particles in the coating is noted as a deformation zone in Fig. 3(b). The region that existed in the gaps of deformation zone shows relatively uniform contrast in the SEM-BSE images, which means that the chemical elements were distributed homogeneously. Therefore, it can be inferred as a single-phase solid solution structure. Combined with XRD results, the FCC supersaturated solid solution was formed by rapid solidification of liquid powders. The chemical composition of regions was analyzed by EDS, as listed in Table 5. There was no significant difference between the two zones, and the element contents were close to the nominal composition of EHEA. It is illustrated that no diffusion or segregation of individual elements occurred in the two zones. Moreover, the O element peak cannot be found in the EDS energy spectrum of coating, and no possible oxides were found in the XRD spectrum. Although the spraying was carried in an atmospheric environment, almost no oxidation occurred in the coatings, which was critical for high cohesion.

The unique characteristics of lower flame temperature and higher impact velocity in HVAF are the critical reasons for the formation of this structure. The fine powders tended to melt when particles were heated in the flame flow. For larger particles, only the powder surface melted or even not melted in short-time heating. The un-melted particles were softened and then deposited on the coating. The molten liquid powders and molten part of the surface filled the gaps of the deformation particles. Under the rapid cooling conditions, a supersaturated solid solution was formed. As a result, the laminated structure of the melt-solidified zone and the deformation zone was obtained. It is worth mentioning that because of thermal stress caused by solidification, the laminated structure of the solidification zone and the deformation zone made the distribution of stress inside the coating very complicated. The inhomogeneous stress led to severe lattice distortion and finally reflected serious diffraction peaks broadening in XRD pattern.

Corrosion Resistance

Figure 4 showed the electrochemical corrosion test of EHEA coating and SUS 304 in 3.5 wt.% NaCl solution. Typical potentiodynamic polarization curves were shown in Fig. 4(a), and relative electrochemical parameters were listed in Table 6. The statistical results showed that the corrosion tendency of EHEA coating (-0.221 ± 0.027

Table 4 Parameters of main peaks in XRD patterns

| 2-Theta	Phase	Coating FWHM	Powder FWHM	Instrumental FWHM
37.7	Laves	0.454	0.204	0.111
41.2	Laves	0.553	0.248	0.109
43.4	FCC	0.569	0.117	0.107
44.5	Laves	0.65	0.344	0.107
45.4	Laves	0.427	0.176	0.106
50.5	FCC	0.878	0.223	0.104
74.3	FCC	1.06	0.227	0.100

Fig. 3 SEM-BSE images of cross-section for EHEA coating: (a) overview; (b) laminated construction of melt-solidified zone and the deformation zone; (c) a partial enlargement of (a) and (insert) high magnification; (d) powder profile and (insert) high magnification
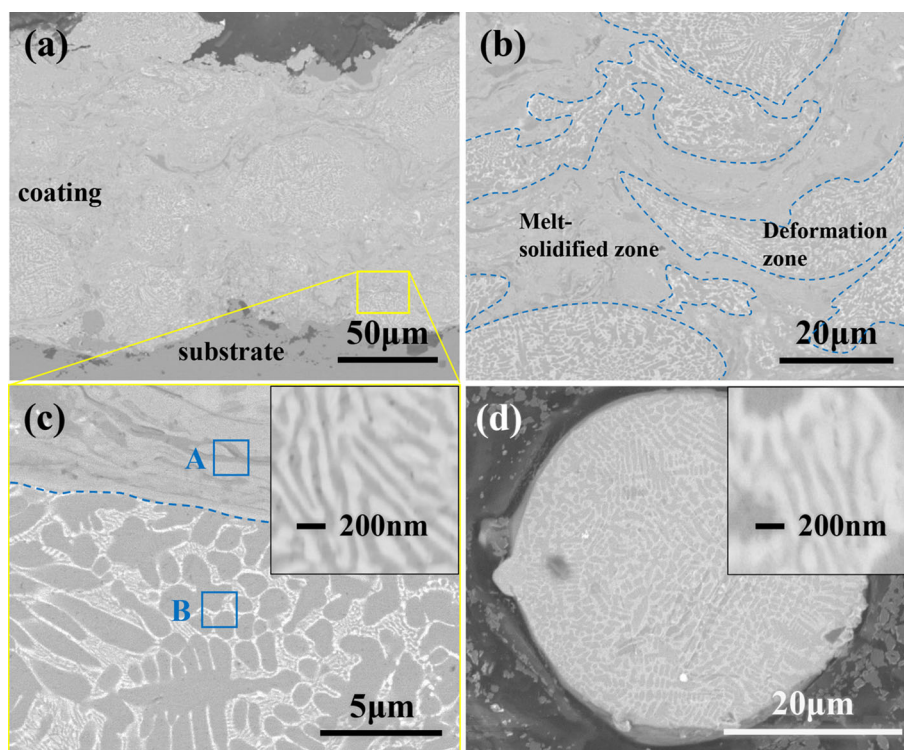
Table 5 Chemical composition of each area of the coating in Fig. 3(c) identified by EDS

Areas	Contents, at.%					
	Al	Cr	Fe	Co	Ni	Ta
A	0.92	20.83	23.88	25.79	21.9	6.68
B	0.19	20.95	25.36	26.91	23.08	3.5

V_{SCE}) was more negative than that of SUS 304 (-0.198 ± 0.014 V_{SCE}), and the corrosion current density of EHEA coating (163.5 ± 25.6 nA/cm^2) was about 1-1.5 times that of SUS 304 (134.4 ± 7.3 nA/cm^2). According to the Nyquist plot (Fig. 5b), the impedance spectrum characteristics of both samples were semi-circle capacitive impedance arc. The arc radius of the EHEA coating was smaller, which means its corrosion resistance was lower (Ref 35).

From Fig. 4(c) we can see that the slope of logz-logf curve of both samples was near −1. The phase angle of phase-logf of EHEA coating and SUS 304 was about 70° and 80°, respectively. It also proves that the corrosion rate of EHEA coating was higher than SUS 304.

According to potentiodynamic polarization curves, there were obvious passivation phenomena in both samples of EHEA coating and SUS 304. The polarization curve of EHEA coating had a stable passivation platform, and the pitting potential was about 0.04 V_{SCE}. By contrast, the passivation platform of SUS 304 was unstable. The surface morphology of each sample after electrochemical corrosion is shown in Fig. 5. It can be seen that the surface of EHEA coating was generally smooth, and the corrosion pits were shallow. The deformed zone of EHEA coating not trigger pitting corrosion as hypo-eutectic structure of this region. Similar studies have demonstrated that the Nanostructured lamellar eutectic oxide film has excellent pitting corrosion
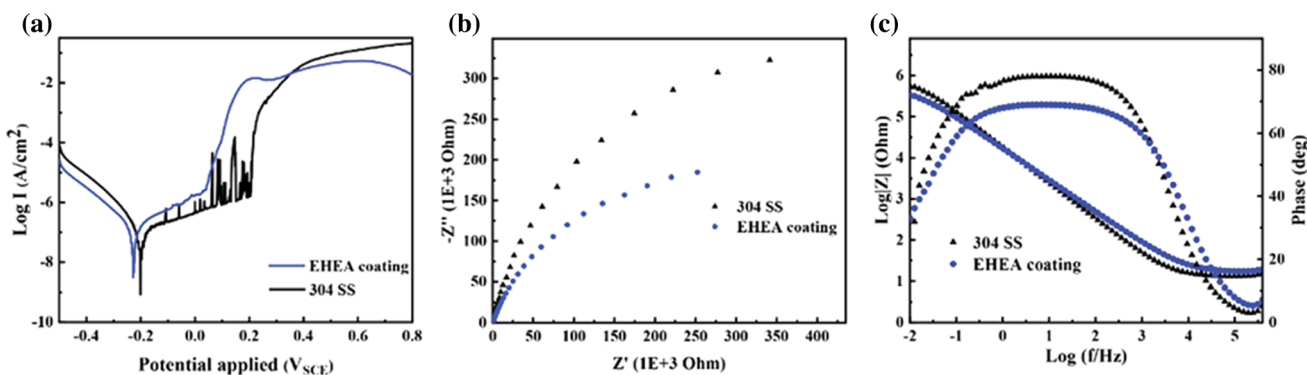
Fig. 4 (a) Typical potentiodynamic polarization curves of EHEA coating and SUS 304 in 3.5 wt.% NaCl solution. (b, c) EIS of EHEA coating and SUS 304 in the single-cylinder corrosion cell under open circuit potential condition: (b) Nyquist plots and (c) Bode plots

Table 6 Electrochemical parameters of EHEA coating and SUS 304 in Fig. 4

Samples	Anodic slopes	Cathodic slopes	E_{corr}, V_{SCE}	I_{corr}, nA/cm^2
EHEA coating	0.221	−0.134	−0.227	158.6
SUS 304	0.416	−0.107	−0.201	135.5

Fig. 5 Corrosion morphologies of EHEA coating (a) and SUS 304 (b)
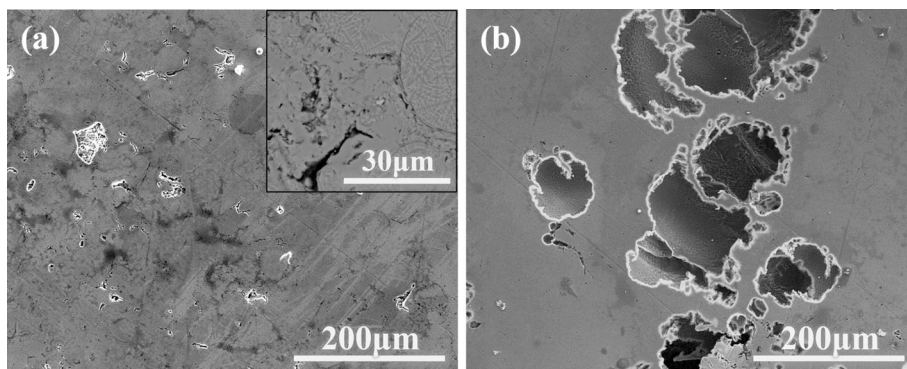
resistance (Ref 22). The localized corrosion of coating mainly occurred at the melt-solidified zone and the boundary of un-melted particles. Microsegregation and other defects may occur in the melt-solidified zone, while stress existed at the boundary of the deformed zone. The passivation film in these areas is more vulnerable to destruction, resulting in localized corrosion. Note that this corrosion resistance weak zone did not occupy the main part of the coating and was separated by the pitting resistance deformed zone. As a result, pitting was blocked in the early development process, and it was difficult to form deep corrosion holes. In contrast, the surface of SUS 304 had severe corrosion holes with a width of nearly 200 μm. Although SUS 304 had a lower corrosion current density, its passivation films were penetrated more easily. This phenomenon corresponded to its unstable potentiodynamic polarization curve. Thus, compared with SUS 304, the EHEA coating had better pitting resistance.

Table 7 Micro-hardness of different samples

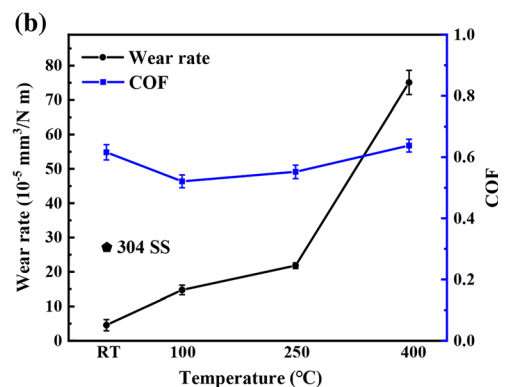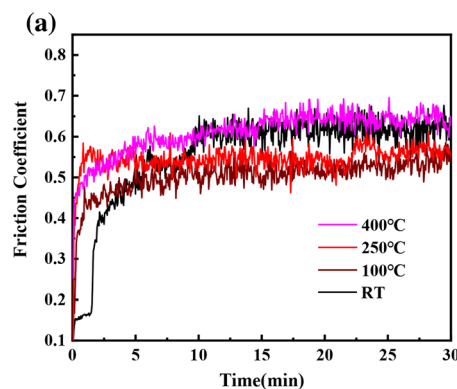| Samples	EHEA coating	As-cast EHEA	SUS 304
HV$_1$	546.6±19.6	390.0±10.6	212.6±10.0

Wear Investigations

The hardness of materials is generally considered to be related to wear resistance, so the microhardness of EHEA coating in cross-section was measured. The result shown in Table 7 revealed that the hardness of the EHEA coating was significantly higher than those of the as-cast EHEA and the SUS 304 substrate. The high hardness of coating was primarily due to the excellent mechanical properties of FCC+Laves eutectic structure and posteriorly to effective solid-solution strengthening in the melt-solidified zone. Moreover, there was a work-hardening effect in the deformed zone. The EHEA coating with high hardness would benefit the protection of matrix materials.

The results of dry wear tests of EHEA coating at different ambient temperatures are shown in Fig. 6. The coefficient of friction (COF) shown in Fig. 6(a) indicated that the COF rapidly reached a stable state at all temperatures with very small fluctuation range shortly after the friction begins. The curve of average COF at the stabilization stage related to environment temperature was shown in Fig. 6 (b). The average COF at 100, 250, and 400 °C were 0.616, 0.521, 0.552, and 0.638, respectively. The lowest COF occurred at 100 °C, while the highest at temperature rose to 400 °C. Figure 6(b) also showed the wear rate of EHEA coating in different conditions. EHEA coating had the best wear resistance at room temperature, with a wear rate of 4.5×10^{-5} mm³/Nm, which was lower than that of SUS 304 (27.1×10^{-5} mm³/Nm) in literature (Ref 36). The excellent wear resistance was consistent with the high hardness of the EHEA coating. Additionally, it can be found that ambient temperature has a significant effect on the wear resistance of EHEA coating. The wear rate below 250 °C increased slowly as the temperature increased. The wear rate at 400 °C increased to 75.1×10^{-5} mm³/Nm. This showed that the EHEA coating had good wear resistance below 250 °C, but severe softening would occur at 400 °C, resulting in a significant decline in wear resistance. Worn surfaces profiles of EHEA coating at different friction temperatures are shown in Fig. 7. It can be found that the higher experimental environment temperature was, the larger the wear width and depth were, and the rougher the surface was, indicating that the wear was more severe. When the temperature rose to 400 °C, the depth of wear profiles increased sharply 65.3 μm. It can be concluded that the plastic deformation resistance of the alloy decreased seriously, resulting in the damage of the material along with the transverse and longitudinal directions of the contact surface.

To explore the wear mechanisms of EHEA coating, we analyzed the worn morphologies and wore debris at various temperatures, as shown in Fig. 8. The first column is the secondary electron image of the worn track, and the second column is the corresponding backscattered electron image.
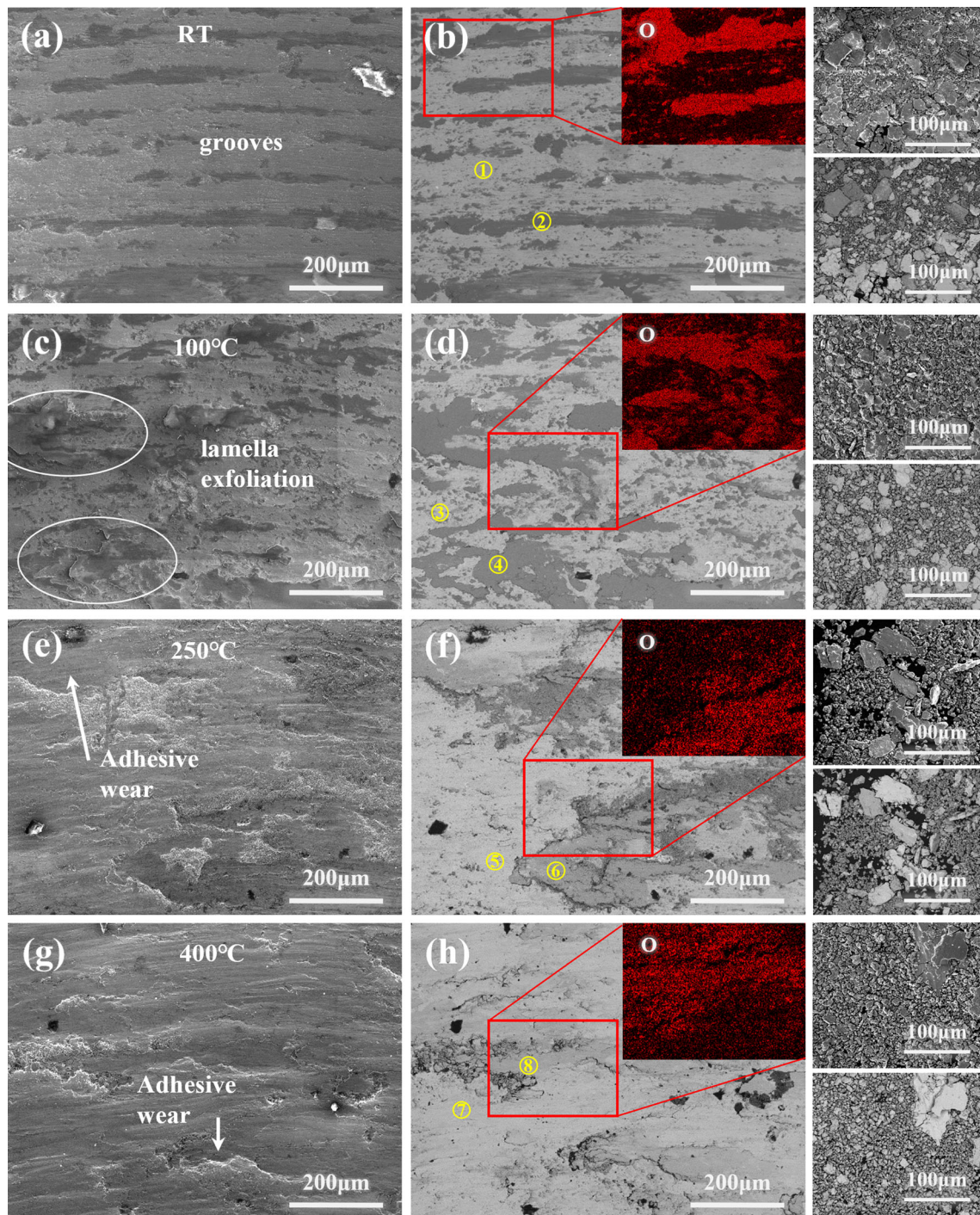
It can be seen from the SE Mode image that there are apparent furrows or grooves on the wear track surface at room temperature, which corresponds to the microscopic cutting mechanism. In addition, a patchy structure also exists, which adheres to the surface of the wear track along the wear direction. EDS mapping of O (the inserted images) and elemental analysis (Table 8) confirm that the patchy structure is an oxide film. The wear debris was mainly formed from sheet structures accompanied by some fine powders. Comparing the SE and BSE images of the debris, it can be found that they contain metal fragments and oxide film. The fragments stripped from the surface and entered the friction pair, forming three-body wear. Therefore, the wear mechanisms of the EHEA coating at room temperature were mainly abrasive wear accompanied by oxidation wear. Due to its high hardness and strong resistance to inelastic shear deformation, the EHEA coating had good wear resistance at room temperature.

The wear morphology at high temperature is different from that at room temperature, indicating that the wear mechanism has changed. At 100 °C, the grooves were still dominant. However, the area covered by oxide film is larger, and flake peeling is found. Correspondingly, the
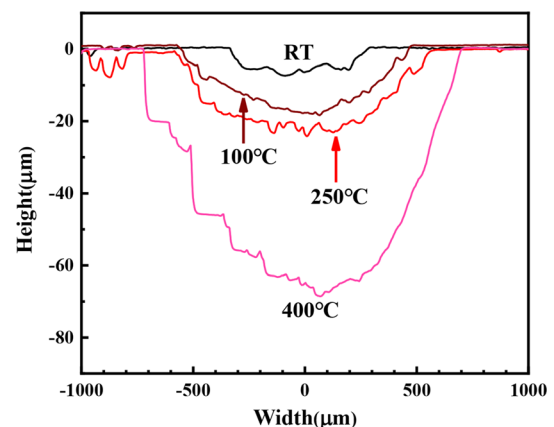
Fig. 7 Worn surfaces profiles of the EHEA coating at different temperatures

Fig. 6 The results of dry wear tests of EHEA coating at different ambient temperatures: (a) COF-time curves; (b) average COF/wear rates temperature (Ref 36)

Fig. 8 Worn morphologies and relative wear debris (attached to the right) of EHEA coating in SE/BSE mode at different temperatures: (a-b) RT, (c-d) 100 °C, (e-f) 250 °C and (g-h) 400 °C; EDS mapping of O (insert)

proportion of oxide film in the chip becomes larger, and the size becomes small. It means that the oxidative wear mechanism is gradually dominant. At higher temperatures, the oxide film on the worn surface becomes less and broken, indicating that it is easy to break and flake. The plastic deformation and cold welding on the wear surface represent adhesive wear. Therefore, the wear mechanisms of the EHEA coating were abrasive and oxidation wear at 100 °C, while adhesive and oxidation wear at elevated temperatures.

It is believed that oxide film is the main factor influencing the wear mechanism at high temperatures, so we investigate the evolution of oxide film. EDS analysis was performed on regions with different contrast degrees in

Table 8 Chemical composition of each region of worn surface in Fig. 8

Regions	Contents, at.%						
	O	Al	Cr	Fe	Co	Ni	Ta
1	6.40	1.24	17.90	22.16	23.81	21.74	6.76
2	69.91	0.70	5.69	6.82	8.05	6.91	1.91
3	8.25	1.27	16.98	21.92	23.54	21.60	6.43
4	67.34	0.84	6.18	7.77	8.42	7.21	2.25
5	4.83	1.51	17.97	22.31	24.56	21.83	6.99
6	52.21	0.81	8.75	11.31	12.64	11.19	3.10
7	10.11	1.84	17.19	20.92	22.81	20.31	6.82
8	36.39	1.13	12.07	14.43	16.97	14.95	4.06

BSE images of wear surfaces at different temperatures, and the results are shown in Table 8. It can be seen that the chemical composition of regions of exposed metal at various temperatures was close to the nominal composition of EHEA. Based on the results in Fig. 6, it can be inferred that the oxide film formed at 100 °C effectively reduces the friction coefficient. Studies have proved that the oxide film generated during high-temperature friction has lubrication and protection effects, which reduced the friction coefficient and wear loss (Ref 36, 37). Above 250 °C, the coating was more likely to oxidize, which is consistent with the wear debris mainly consists of oxide film. However, according to BSE images and O element EDS mappings, it can be seen that the oxide film on the worn surface became broken at high temperatures. This phenomenon becomes more pronounced as temperatures rise. This explains the decrease in the content of O element in the oxide film on the friction surface at 250 and 400 °C, as shown in Table 8. We can judge that the oxide film is more likely to break and flake off at high temperatures so that oxide film can hardly be observed in the wear track at 250 and 400 °C. In this case, the rapidly forming and peeling oxide film no longer reduces friction, leading to the increase of friction coefficient at high temperatures.

On the other hand, the high temperature would weaken the complex stress field of the coating and the work hardening of the deformed zone. Moreover, FCC phase, the main component of the EHEA coating, is more likely to soften at high temperatures. All of these result in the decrease of the plastic shear deformation resistance of the coating and aggravate the adhesive wear. Therefore, high temperatures exacerbate both forms of wear, leading to a sharp increase in coating wear rates.

Conclusions

In order to understand the surface protection of traditional structural materials under the combined action of corrosion and friction, non-equiatomic CoCrFeNiTaAl EHEA coating was produced on SUS 304 substrate by HVAF using gas atomized feedstock. The following conclusions are obtained.

1. The EHEA coating with a dense and non-oxidized structure was obtained. In the process of HVAF, only part of the powders melted, and the rest was deposited through solid deformation. The coating was composed of a deformation zone and a melt-solidified zone. The deformation zone had the same structure as the original powders of hypo-eutectic structure, while the melt-solidified zone of a single-phase solid solution structure.

2. The corrosion current density of EHEA coating in 3.5 wt.% NaCl solution was 36% higher than SUS 304. EHEA coating has better pitting resistance due to the eutectic structure of the deformation zone in the coating. Although the melt-solidified zone was a weak area for corrosion, its discontinuous structure made it difficult for pitting to expand further.

3. The wear resistance of EHEA coating is better than SUS 304 at RT and decreases with the increase of temperature. The EHEA coating showed abrasive and oxidation wear mechanism at RT and 100 °C, while oxidation and adhesive wear at elevated temperatures. The oxidation film of EHEA coating was easier to peel off at high temperatures, which made oxidation wear severe.

The considerable pitting resistance and wear resistance at room temperature of EHEA coatings demonstrate excellent potential for the protection of moving parts in 3.5 wt.% NaCl environment.

References

1. N.J. Wagner, W.W. Gerberich and J.V.R. Heberlein, Thermal Plasma Chemical Vapor Deposition of Wear-Resistant, Hard Si-C-N Coatings, *Surf. Coat. Technol.*, 2006, **201**(7), p 4168-4173.

2. K. Hou and Y. Chen, Preparation and Wear Resistance of Pulse Electrodeposited Ni-W/Al_2O_3 Composite Coatings, *Appl. Surf. Sci.*, 2011, **257**(15), p 6340-6346.

3. F. Movassagh-Alanagh, A. Abdollah-zadeh, M. Aliofkhazraei and M. Abedi, Improving the Wear and Corrosion Resistance of Ti-6Al-4V alloy by Deposition of TiSiN Nanocomposite Coating with Pulsed-DC PACVD, *Wear*, 2017, **390-391**, p 93-103.

4. Y. Zhang, T.T. Zuo, Z. Tang, M.C. Gao, K.A. Dahmen, P.K. Liaw and Z.P. Lu, Microstructures and Properties of High-Entropy Alloys, *Prog. Mater Sci.*, 2014, **61**, p 1-93.

5. B. Liu, J. Wang, Y. Liu, Q. Fang, Y. Wu, S. Chen and C.T. Liu, Microstructure and Mechanical Properties of Equimolar FeCoCrNi High Entropy Alloy Prepared via Powder Extrusion, *Intermetallics*, 2016, **75**, p 25-30.

6. B. Cai, B. Liu, S. Kabra, Y. Wang, K. Yan, P.D. Lee and Y. Liu, Deformation Mechanisms of Mo Alloyed FeCoCrNi High Entropy Alloy: In Situ Neutron Diffraction, *Acta Mater.*, 2017, **127**, p 471-480.

7. Y.Y. Chen, U.T. Hong, H.C. Shih, J.W. Yeh and T. Duval, Electrochemical Kinetics of the High Entropy Alloys in Aqueous Environments—A Comparison with type 304 Stainless Steel, *Corros. Sci.*, 2005, **47**(11), p 2679-2699.

8. Y.L. Chou, J.W. Yeh and H.C. Shih, The Effect of Molybdenum on the Corrosion Behaviour of the High-Entropy Alloys $Co_{1.5}CrFeNi_{1.5}Ti_{0.5}Mox$ in Aqueous Environments, *Corros. Sci.*, 2010, **52**(8), p 2571-2581.

9. C.L. Wu, S. Zhang, C.H. Zhang, H. Zhang and S.Y. Dong, Phase Evolution and Cavitation Erosion-Corrosion Behavior of $FeCoCrAlNiTi_x$ High Entropy Alloy Coatings on 304 Stainless Steel by Laser Surface Alloying, *J. Alloys Compd.*, 2017, **698**, p 761-770.

10. C. Huang, Y. Zhang, R. Vilar and J. Shen, Dry Sliding Wear Behavior of Laser Clad TiVCrAlSi High Entropy Alloy Coatings on Ti-6Al-4V Substrate, *Mater. Des.*, 2012, **41**, p 338-343.

11. W. Wu, L. Jiang, H. Jiang, X. Pan, Z. Cao, D. Deng, T. Wang and T. Li, Phase Evolution and Properties of $Al2CrFeNiMox$High-Entropy Alloys Coatings by Laser Cladding, *J. Therm. Spray Technol.*, 2015, **24**(7), p 1333-1340.

12. C.L. Wu, S. Zhang, C.H. Zhang, H. Zhang and S.Y. Dong, Phase Evolution and Properties in Laser Surface Alloying of $FeCoCrAlCuNix$ High-Entropy Alloy on Copper Substrate, *Surf. Coat. Technol.*, 2017, **315**, p 368-376.

13. J. Wang, B. Zhang, Y. Yu, Z. Zhang, S. Zhu, X. Lou and Z. Wang, Study of High Temperature Friction and Wear Performance of $(CoCrFeMnNi)_{85}Ti_{15}$ High-Entropy Alloy Coating Prepared by Plasma Cladding, *Surf. Coat. Technol.*, 2020, **384**, p 125337.

14. M. Löbel, T. Lindner and T. Lampke, High-Temperature Wear Behaviour of $AlCoCrFeNiTi_{0.5}$ Coatings Produced by HVOF, *Surf. Coat. Technol.*, 2020, **403**, p 126379.

15. D. Zhao, T. Yamaguchi, D. Tusbasa and W. Wang, Fabrication and Friction Properties of the AlFeCrCo Medium-Entropy Alloy Coatings on Magnesium Alloy, *Mater. Des.*, 2020, **193**, p 108872.

16. B. Ren, Z.X. Liu, D.M. Li, L. Shi, B. Cai and M.X. Wang, Corrosion Behavior of CuCrFeNiMn High Entropy Alloy System in 1 M Sulfuric Acid Solution, *Mater. Corros.*, 2015, **63**(9), p 828-834.

17. Y. Guo and Q. Liu, MoFeCrTiWAlNb Refractory High-Entropy Alloy Coating Fabricated by Rectangular-Spot Laser Cladding, *Intermetallics*, 2018, **102**, p 78-87.

18. L.X. Han, C.M. Wang and H.F. Sun, Microstructure and Anti-corrosion Property of High-Entropy alloy $AlFeNiCrCoTi_{0.5}V_x$, *Mater. Trans.*, 2016, **57**(7), p 1134-1137.

19. X.L. Shang, Z.J. Wang, Q.F. Wu, J.C. Wang, J.J. Li and J.K. Yu, Effect of Mo Addition on Corrosion Behavior of High-Entropy Alloys $CoCrFeNiMo_x$ in Aqueous Environments, *Acta Metall. Sin. (Engl. Lett.)*, 2019, **32**(1), p 41-51.

20. Y. Lu, Y. Dong, S. Guo, L. Jiang, H. Kang, T. Wang, B. Wen, Z. Wang, J. Jie, Z. Cao, H. Ruan and T. Li, A Promising New Class of High-Temperature Alloys: Eutectic High-Entropy Alloys, *Sci. Rep.*, 2014, **4**, p 6200.

21. Y. Lu, Y. Dong, H. Jiang, Z. Wang, Z. Cao, S. Guo, T. Wang, T. Li and P.K. Liaw, Promising Properties and Future Trend of Eutectic High Entropy Alloys, *Scr. Mater.*, 2020, **187**, p 202-209.

22. S. Shuang, Z.Y. Ding, D. Chung, S.Q. Shi and Y. Yang, Corrosion Resistant Nanostructured Eutectic High Entropy Alloy, *Corros. Sci.*, 2020, **164**, p 108315.

23. Y. Yu, F. He, Z. Qiao, Z. Wang, W. Liu and J. Yang, Effects of Temperature and Microstructure on the Triblogical Properties of $CoCrFeNiNb_x$ Eutectic High Entropy Alloys, *J. Alloys Compd.*, 2019, **775**, p 1376-1385.

24. H. Jiang, Study on Composition Design and Mechanical Properties of CoFeNi(Cr)-M Eutectic High Entropy Alloys, Dalian University of Technology, 2018.

25. L. Han, X. Xu, Z. Li, B. Liu, C.T. Liu and Y. Liu, A Novel Equiaxed Eutectic High-Entropy Alloy with Excellent Mechanical Properties at Elevated Temperatures, *Mater. Res. Lett.*, 2020, **8**(10), p 373-382.

26. D. Lin, N. Zhang, B. He, B. Jin, Y. Zhang, D. Li and F. Dong, Influence of Laser Re-melting and Vacuum Heat Treatment on Plasma-Sprayed FeCoCrNiAl Alloy Coatings, *J. Iron. Steel Res. Int.*, 2017, **24**(12), p 1199-1205.

27. Q. Ye, K. Feng, Z. Li, F. Lu, R. Li, J. Huang and Y.J.A.S.S. Wu, Microstructure and Corrosion Properties of CrMnFeCoNi High Entropy Alloy Coating, *Appl. Surf. Sci.*, 2017, **396**(PT.2), p 1420-1426.

28. T. Li, Y. Liu, B. Liu, W. Guo and L. Xu, Microstructure and Wear Behavior of $FeCoCrNiMo_{0.2}$ High Entropy Coatings Prepared by Air Plasma Spray and the High Velocity Oxy-Fuel Spray Processes, *Coatings*, 2017, **7**(9), p 151.

29. L. Chen, K. Bobzin, Z. Zhou, L. Zhao, M. Öte, T. Königstein, Z. Tan and D. He, Wear Behavior of HVOF-Sprayed $Al_{0.6}TiCrFeCoNi$ High Entropy Alloy Coatings at Different Temperatures, *Surf. Coat. Technol.*, 2019, **358**, p 215-222.

30. J. Xiao, Y. Wu, J. Chen and C. Zhang, Microstructure and Tribological Properties of Plasma Sprayed $FeCoNiCrSiAl_x$ High Entropy Alloy Coatings, *Wear*, 2020, **448-449**, p 203209.

31. E. Sadeghimeresht, N. Markocsan and P. Nylén, A Comparative Study on Ni-Based Coatings Prepared by HVAF, HVOF, and APS Methods for Corrosion Protection Applications, *J. Therm. Spray Technol.*, 2016, **25**(8), p 1604-1616.

32. R.E. Kumar, M. Kamaraj, S. Seetharamu and S. Anand Kumar, A Pragmatic Approach and Quantitative Assessment of Silt Erosion Characteristics of HVOF and HVAF Processed WC-CoCr Coatings and 16Cr5Ni Steel for Hydro Turbine Applications, *Mater. Des.*, 2017, **132**, p 79-95.

33. J. Li, W. Jia, J. Wang, H. Kou, D. Zhang and E. Beaugnon, Enhanced Mechanical Properties of a CoCrFeNi High Entropy Alloy by Supercooling Method, *Mater. Des.*, 2016, **95**, p 183-187.

34. L. Avril, B. Courant and J.J. Hantzpergue, Tribological Performance of α-Fe(Cr)-Fe_2B-FeB and α-Fe(Cr)-h-BN Coatings Obtained by Laser Melting, *Wear*, 2006, **260**(4), p 351-360.

35. X. Cui, X. Lin, C. Liu, R. Yang, X. Zheng and M. Gong, Fabrication and Corrosion Resistance of a Hydrophobic Micro-arc Oxidation Coating on AZ31 Mg Alloy, *Corros. Sci.*, 2015, **90**, p 402-412.

36. C. OuYang, X. Liu, Y. Luo, J. Liang, M. Wang and D. Chen, Preparation and High Temperature Tribological Properties of Laser In-Situ Synthesized Self-lubricating Composite Coating on 304 Stainless Steel, *J. Market. Res.*, 2020, **9**(4), p 7034-7046.

37. H. Torres, M. Rodríguez Ripoll and B. Prakash, Tribological Behaviour of Self-lubricating Materials at High Temperatures, *Int. Mater. Rev.*, 2018, **63**(5), p 309-340.